

Strain rate and fuel composition dependence of chemiluminescent species profiles in non-premixed counterflow flames: comparison with model results

B. Prabasena · M. Röder · T. Kathrotia · U. Riedel ·
T. Dreier · C. Schulz

Received: 4 October 2011 / Revised version: 20 January 2012 / Published online: 30 March 2012
© Springer-Verlag 2012

Abstract A detailed comparison has been conducted between chemiluminescence (CL) species profiles of OH^* , CH^* , and C_2^* , obtained experimentally and from detailed flame kinetics modeling, respectively, of atmospheric pressure non-premixed flames formed in the forward stagnation region of a fuel flow ejected from a porous cylinder and an air counterflow. Both pure methane and mixtures of methane with hydrogen (between 10 and 30 % by volume) were used as fuels. By varying the air-flow velocities methane flames were operated at strain rates between 100 and 350 s^{-1} , while for methane/hydrogen flames the strain rate was fixed at 200 s^{-1} . Spatial profiles perpendicular to the flame front were extracted from spectrograms recorded with a spectrometer/CCD camera system and evaluating each spectral band individually. Flame kinetics modeling was accomplished with an in-house chemical mechanism including C_1 – C_4 chemistry, as well as elementary steps for the formation, removal, and electronic quenching of all measured active species. In the CH_4/air flames, experiments and model results agree with respect to trends in profile peak intensity and position. For the $\text{CH}_4/\text{H}_2/\text{air}$ flames, with increasing H_2 content in the fuel the experimental CL peak intensities decrease slightly and their peak positions shift towards the fuel side, while for the model the drop in mole fraction is much stronger and the peak positions move closer

to the fuel side. For both fuel compositions the modeled profiles peak closer to the fuel side than in the experiments. The discrepancies can only partly be attributed to the limited attainable spatial resolution but may also necessitate revised reaction mechanisms for predicting CL species in this type of flame.

1 Introduction

For decades strained, laminar, non-premixed counterflow flames have received much attention in combustion science, and there have been numerous theoretical and experimental studies of their structure, extinction behavior, species composition, and temperature [1–4], as well as their chemiluminescence (CL) emission [5]. Counterflow flames also lend their importance from being one successful approach for turbulent premixed combustion modeling, which is based on treating the flame front as being composed of flamelets where fuel and oxidizer streams mix in a diffusion layer, and the macroscopic flame front is reconstructed from such flamelets of various strain and curvature [6]. Partially premixed counterflow flames—where a fuel-rich premixed flame provides preheated fuel/combustion gases to an outer diffusion layer with a counterflowing air stream—have also been investigated [7].

Due to its natural occurrence, ease of detection, and since it is an optical, non-intrusive diagnostic, CL from flames is widely used in a variety of combustion studies. These include localization of the reaction zones [8, 9], as a marker of local heat-release rate [9, 10], and for the measurement of equivalence ratios [10–14]. CL also provides prospects for active combustion control [15]. Often, the ratios of CL intensities from different species (e.g. OH^*/CH^* , C_2^*/CH^*) are evaluated because they provide a monotonic variation

B. Prabasena · M. Röder · T. Dreier (✉) · C. Schulz
IVG, Institute for Combustion and Gasdynamics,
University of Duisburg-Essen, 47048 Duisburg, Germany
e-mail: thomas.dreier@uni-due.de
Fax: +49-203-3793087

T. Kathrotia · U. Riedel
University of Stuttgart and Institute of Combustion Technology,
German Aerospace Center (DLR), Pfaffenwaldring 38–40,
70569 Stuttgart, Germany

as a function of equivalence ratio (within a limited range) independent of the total fuel mass flow [12, 14]. The measurement of these CL ratios also reduces the dependence of these data on parameters such as strain rate, type of fuel, and heat-release rate.

In most of the cited works, CL emissions were collected globally from the flames, i.e. by spatially integrating detection. Although experimentally much simpler, this method reduces the detail of information obtainable from such data with respect to spatial variations in the flame parameters. Spatially resolved measurements were performed with a CL sensor based on a Cassegrain optics and fast photodetectors by Akamatsu et al. [8], Hardalupas et al. [9], and Kojima et al. [16]. Previously, Hardalupas and Orain [10] showed that in premixed counterflow flames at atmospheric pressure the OH^*/CH^* CL-intensity ratio has a non-monotonic dependence on equivalence ratio independent of strain rate, in contrast to the C_2^*/OH^* ratio, which is a function of strain rate. Recently, good quantitative agreement between measured spatial profiles of absolute species concentrations of OH^* and CH^* and model predictions has been achieved by De Leo et al. [5] in flat opposed-flow CH_4/O_2 non-premixed flames with low strain rates between 20 and 40 s^{-1} and with O_2 concentrations on the oxidizer side between 21 and 100 %.

A deeper understanding of the chemical routes leading to the formation and destruction of electronically excited species in flames can be gained through chemical kinetics modeling of the combustion process. Despite the broad use of CL as combustion diagnostics, there has been limited research along these lines, starting with Dandy and Vosen [17], where modeling the formation of OH^* CL was combined with experiments in lean premixed CH_4/air flames. Walsh et al. [18] proposed a CL mechanism and compared the simulations with measured OH^* mole fractions for a lifted laminar axisymmetric non-premixed flame, while Luque et al. [19] adjusted the rate constant for OH^* formation in that mechanism for improving its performance to better match the excited species profiles in flames. Including radiation corrections, Samaniego et al. [20] carried out detailed flame modeling for methane and propane/air flames to elucidate the role of the CO_2^* -CL intensities in quantifying their relationship to the heat-release rate and fuel-consumption rate, respectively, with respect to variations of strain and unsteadiness.

Panoutsos et al. [11] numerically evaluated equivalence-ratio measurements using OH^* - and CH^* -CL in premixed and non-premixed CH_4/air flames in a counterflow configuration, and tested the performance of different detailed CH_4 -oxidation mechanisms that account for the formation and destruction of OH^* and CH^* . In premixed laminar CH_4/air flames at atmospheric pressure the authors also studied the

effect of equivalence ratio and strain rate on the CL intensity as well as on OH^*/CH^* -CL intensity ratios. The computational results were compared with measured absolute data, and they assessed the validity of using the CL intensity of OH^* and CH^* as heat-release-rate markers. Pure non-premixed flames like the ones described in our work below were not investigated by these authors. Also, since the partial replacement of hydrocarbons by hydrogen is an interesting option for future energy conversion systems with partial replacement of fossil fuels, operating the current burner with H_2 -containing fuels is of interest for better understanding of the performance of fuel-flexible combustion systems.

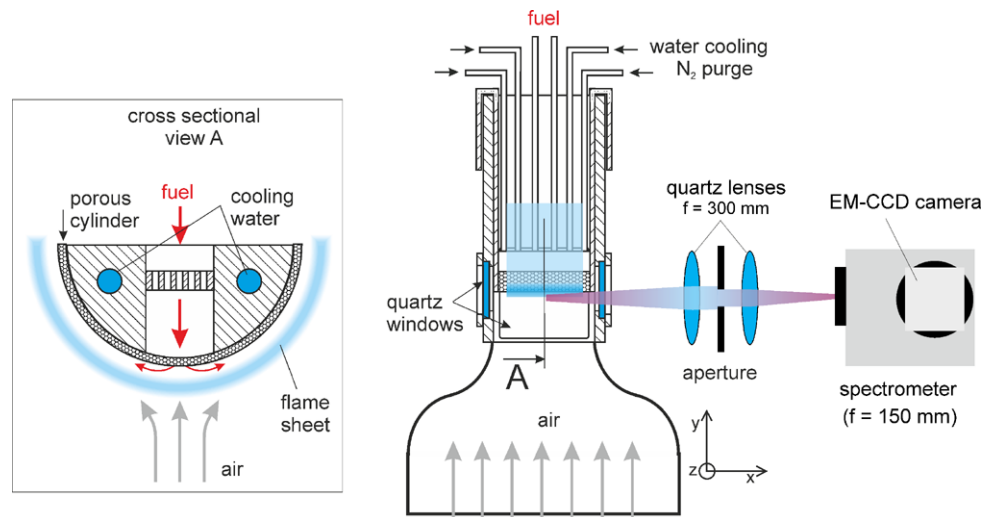
The majority of investigations listed above focused on premixed or partially premixed flames, while experiments with accompanying flame modeling for non-premixed, counterflow flames are rarely reported. To fill this gap, we present a detailed comparison of measured spatially resolved CL-intensity profiles and simulated mole-fraction profiles of the main CL species OH^* , CH^* , and C_2^* using a comprehensive flame mechanism. Measurements were performed by spectrally and spatially resolved detection of chemiluminescence across the flame front of non-premixed counterflow flames using CH_4 and CH_4/H_2 as fuels, and operated with various strain rates. Because the mechanism does not treat soot formation, non-sooting flames were investigated only.

2 Experimental procedures

2.1 Non-premixed counterflow burner and chemiluminescence detection

All experiments were performed using a non-premixed counterflow burner of the 'Tsuji type' [1, 4, 21] as depicted in Fig. 1 (center and left-hand panels). The fuel is delivered from above into a water-cooled copper cylinder (length: 80 mm, outer diameter: 40 mm) with a rectangular ($10 \times 60 \text{ mm}^2$ slot) mixing chamber (cross section: left-hand panel in Fig. 1), where it first passes through a perforated plate to enhance mixing in the lower part of the chamber. The gas then exits through a porous sintered half-cylinder shell (porosity B20, wall thickness: 2 mm) covering the lower part of the fuel cylinder into the counterpropagating air flow. The air flow is delivered by four fans mounted at the bottom of a square-shaped flow duct with converging nozzle (center panel of Fig. 1). Two additional flow ports at both ends of the fuel channel (separated from the latter by 0.5-mm-thick copper plates) provide a small coflow of dry nitrogen to extinguish the flame attached at both ends, thus providing a straight horizontal flame sheet standing off the cylinder surface and along the optical viewing direction of the CL detection system (depicted in the right-hand panel of Fig. 1).

Fig. 1 Non-premixed counterflow burner (*center*): depicted is the upper section of the air-flow duct with the converging nozzle, the optically accessible combustion chamber, and the vertically translatable fuel cylinder. *Left-hand panel*: cross section through the fuel cylinder, showing schematically the porous sintered half-cylinder plate and the flame front. *Right-hand panel*: CL imaging optics, spectrometer, and electron-multiplication CCD camera



The center panel in Fig. 1 schematically shows the cross section of the upper part of the burner with the converging air-flow duct and the square-shaped ($100 \times 100 \text{ mm}^2$) combustion chamber. The fuel cylinder is mounted on a translation stage (MICOS, VT80; not shown in Fig. 1) to enable vertical positioning with a precision of $10 \mu\text{m}$ within the window ports in each of the four side walls. The combustion chamber is attached to the air-flow duct (square-shaped cross section, 250-mm side length, 1000-mm long) via the converging nozzle. Together with several fine-wire meshes on top and bottom of a 100-mm-thick block of honeycomb structure 500 mm upstream the nozzle, this generates a laminar flow with a top-hat velocity profile at its exit. Spatial profiles of the air velocity recorded with a hot-wire anemometer (DISA) across the nozzle exit inside the combustion chamber were essentially flat. Global flow velocities were additionally calibrated against a commercial hand-held hot-wire anemometer (Testo) as a function of voltage applied to the four fans. The volumetric flow of fuel and nitrogen through the fuel cylinder was regulated by electronic flow controllers (Bronkhorst), while the required cooling water through the fuel cylinder and through the cooling plates positioned in the exhaust flow on either side of the gas supply tubing (not shown in Fig. 1) was regulated to 60°C by a thermostat. These cooling plates simultaneously avoided turbulent wake flow behind the cylinder.

The strain rate, i.e. the stagnation velocity gradient [21], a , defined here as $a = 2v_{\text{air}}/r$, with r the radius of the burner-head fuel cylinder, was varied by changing the speed, v_{air} , of the incoming air. In the experiment, $d = 40 \text{ mm}$; thus, a is numerically equal to the air-flow velocity. Pure non-premixed CH_4/air flames (termed ‘type I’ flames in the following) were operated with strain rates between 100 and 350 s^{-1} . In addition, mixtures of CH_4 with an increasing percentage (by volume) of H_2 (termed ‘type II’ flames) were investigated at a constant strain rate of 200 s^{-1} . In this lat-

ter case the total volumetric fuel flow was kept constant at 3 slpm (standard liters per minute). The burner operating conditions for the present experiments are listed in Table 1.

2.2 Spectrally and spatially resolved chemiluminescence measurements

2.2.1 Chemiluminescence measurements

Spectrally resolved chemiluminescence (CL) radiation was detected with the setup depicted in the right-hand panel of Fig. 1. With the current burner configuration, flame conditions can be considered as one dimensional (1D) along the stagnation stream line. Also, due to the burner geometry, flame parameters do not change along lines parallel to the cylinder axis. Therefore, the measurements that integrate the signal along the line-of-sight were carried out along a vertical plane that contains both the axis of rotational symmetry of the fuel cylinder and the burner centerline. Two 50-mm-diameter quartz lenses, an achromat ($f = 300 \text{ mm}$, Halle), and a $f = 200 \text{ mm}$ plano-convex lens were used to image the center region of the flame onto the entrance slit of an imaging spectrograph (ARC, SpectraPro-150) whose slit height was oriented vertically (i.e. parallel to the burner centerline). A 10-mm-diameter aperture was placed between both lenses to increase the depth of field and thus reduce much of the blurring of the recorded CL profiles created by out-of-focus CL radiation along the luminous flame zone within the line-of-sight of the imaging system. An electron-multiplication (EM) CCD camera (Andor Technology, iXon DV887) with a 512×512 pixel sensor ($16 \times 16 \mu\text{m}^2$ pixel size) was mounted in the exit plane of the spectrometer such that pixel rows and columns were oriented along the wavelength axis and the air free-stream direction, respectively. The overall spatial dispersion along the slit height was $22 \mu\text{m}/\text{pixel}$, as determined by imaging a back-illuminated

Table 1 Operating conditions of the non-premixed counterflow flames investigated in the present study. In all flames the air flows were diluted with less than 1 % Ar (by volume, third column). ${}^\circ V_{\text{air}}^0$: volumetric air

flow converted to standard conditions (273 K, 1013 mbar); $x_{w,x}$: mole fraction of fuel species x ; ${}^\circ V_w$: volumetric fuel flow at the temperature of the fuel cylinder; v_w : fuel exit velocity

Air side			Fuel side				Coflow	
a [s ⁻¹]	${}^\circ V_{\text{air}}^0$ [slm]	${}^\circ V_{\text{Ar}}^0$ [slm]	${}^\circ V_{\text{fuel}}^0$ [slm]	$x_{w_{\text{CH}_4}}$	$x_{w_{\text{H}_2}}$	${}^\circ V_w$ [l/min]	v_w [m/s]	$\overline{\text{N}_2}$ [slm]
100	549	1.24	3	1	0	5.49	0.16	0.50
150	824	1.24	3	1	0	5.49	0.16	0.50
200	1099	1.24	3	1	0	5.49	0.16	0.50
250	1374	1.24	3	1	0	5.49	0.16	0.50
300	1649	1.24	5	1	0	9.15	0.27	0.83
350	1925	1.24	5	1	0	9.15	0.27	0.83
200	1099	1.24	3	0.9	0.1	5.49	0.16	0.50
200	1099	1.24	3	0.8	0.2	5.49	0.16	0.50
200	1099	1.24	3	0.7	0.3	5.49	0.16	0.50

Plexiglas ruler as a target placed in the center of the burner housing (object plane).

With the given imaging system and the 300 l/mm grating in a fixed position a wavelength range between 260 and 400 nm and a spatial extent in the object plane of 7 mm were imaged, respectively, on the CCD sensor. Wavelength calibration was performed by placing a Hg/Ar Pen-Ray discharge lamp (LOT) in front of the entrance slit. In the flame experiments the slit opening was 0.3 mm, and the exposure time of the camera was between 500 and 1500 ms depending on light flux. This allowed the CL bands of OH* ($A^2\Sigma^+ - X^2\Pi$ (1-0) band at 285 nm and (1-1, 0-0) band at 308 nm) and CH* ($A^2\Delta - X^2\Pi$ (1-0) band at 388 nm) to be observed simultaneously. For recording the CH* $A^2\Delta - X^2\Pi$ (0-0) band at 431 nm and the C₂* $A^3\Pi - X^2\Pi$ (1-0) band head at 473 nm the grating was repositioned, and the resulting images were combined in a post-processing step.

2.2.2 Characterization of the imaging system depth-of-field

In the current experiments the chemiluminescence emission is homogeneously distributed along lines parallel to the flame front, which is located parallel to the line-of-sight of the detection system (see Fig. 1). The lens system in front of the spectrometer is adjusted to generate a focused image of the flame-front region from the center of the combustion chamber onto the entrance slit of the spectrometer. The spectrometer slit is positioned parallel to the air-flow direction in the center of the fuel cylinder. The imaging spectrometer therefore detects 1D CL profiles across the flame. However, radiation originating from regions of the flame surface in front of and behind the probe volume focal position also reaches the detector and generates overlapping CL profiles with a variable degree of broadening (depending on the distance of the signal relative to the focal point). An impression

of this broadening effect can be obtained from an estimate of a ‘point-spread imaging function’ when a point-size light source positioned at various locations along the line-of-sight of the imaging system is imaged. Therefore, the spatial blurring and peak intensity variation of an illuminated optical fiber (50- μm core diameter) in the image plane (i.e. the location of the camera sensor) were investigated for different distances from the focus position. The input of the optical fiber was illuminated by a UV discharge lamp and the other end was mounted on a motorized translation stage (MICOS, VT80) and translated along the optical axis of the detector through the center of the combustion chamber. Images of the fiber output were recorded for several positions.

Figure 2 shows a series of vertical intensity profiles (white lines in the three sample images shown to the left of the graph) across the registered blurred spot images for several fiber positions. It is observed that, as expected for a focused imaging setup, the larger the distance of the fiber end from the focal point position of the imaging system (here, for a nominal distance of 30 mm on the optical axis), the larger the width of each profile and the smaller of its peak intensity. As can be seen in the left-hand column of the fiber spot images, because the detection through the 1D slit becomes less efficient with increasing size of the (two-dimensional) spot, the total signal contribution decreases with increasing distance from the focus location. As an estimate of the spatial resolving power of the present imaging system, the smallest full width at half maximum (FWHM) of the spot profiles in Fig. 2 amounts to 220 μm .

2.2.3 Processing of image spectrograms

The raw image spectrograms show spatial information on the y-axis and spectral information on the x-axis. After subtracting a background image measured without the flame,

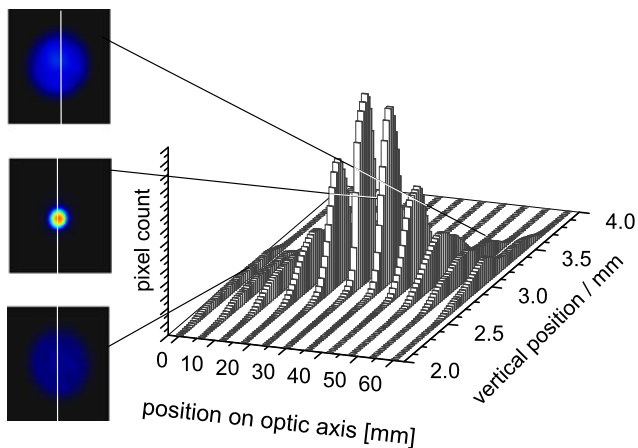


Fig. 2 Analysis of the line-of-sight imaging characteristics of the CL-detection system: intensity profiles along the vertical white pixel columns (indicated in the left-hand sample images) of the blurred image of the fiber output when located at several positions along the optical axis inside the combustion chamber. See text for further explanations

four neighboring horizontal rows were binned together (resulting in a spatial dispersion of $88 \mu\text{m}/\text{pixel}$) to enhance the signal-to-noise in the spectrograms, while the spectral dimension (x -axis) was smoothed by a median filter. A typical CL spectrum from such a ‘super pixel’ row is depicted in Fig. 3 (black line). The prominent individual bands of OH^* , CH^* , and C_2 are clearly visible above a broad unstructured background, which commonly is attributed to CL from CO_2^* , HCO^* , and H_2CO^* [22, 23]. A spectrally smooth section between 330 and 370 nm, which is considered as due to the CO_2^* -continuum emission [20], was evaluated as CL signal from this species. The spectral bands of interest were further processed by linearly interpolating the background intensity between manually set wavelength boundaries (drop-down lines in Fig. 3), whose contribution was subsequently subtracted from the raw spectrum (red line). For each spatial position (i.e. pixel row) the individual chemiluminescence bands were then evaluated by fitting their shape with a spline function and determining, respectively, their integrated band intensity (hatched areas between selected wavelength boundaries in Fig. 3) and peak intensities.

3 Modeling

The kinetics mechanism used in this work consists of a basic C_1 – C_4 hydrocarbon mechanism with an additional CL sub-model. The basic mechanism was recently documented in the PhD thesis of one of the authors [24]. This mechanism describes the oxidation of hydrocarbons for non-sooting flame conditions. The CL sub-model requires, in addition to the chemiluminescent species, elementary reactions for

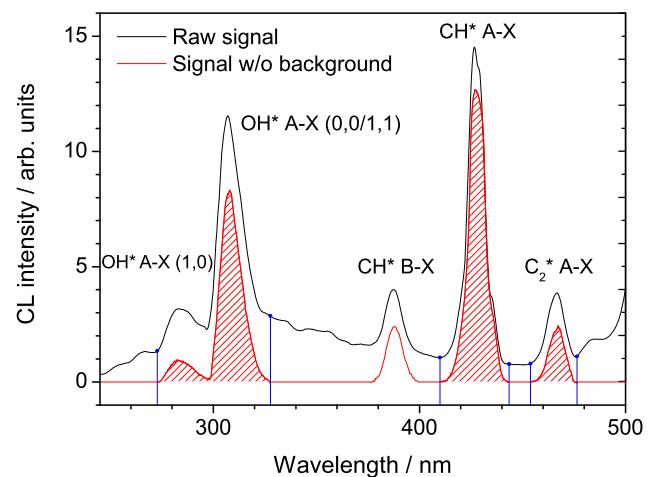


Fig. 3 Typical raw CL spectrum (black line) and background-subtracted spectrum (red line). Selected spectral band boundaries and processed bands are indicated as blue drop-down lines and hatched areas, respectively

C , C_2 , and C_3 species which are important for predicting CH^* and C_2^* . The entire mechanism contains 68 species and 924 (forward and backward) elementary reactions. The kinetics of the chemiluminescent species is described by the formation reactions where the excited-state species are formed from energy-rich intermediates and the consumption reactions, i.e. radiative decay or collisional deactivation. The thermochemical data are taken from the Goos–Burcat–Ruscic database [25]. The sub-mechanism for excited species with additional reactions of C , C_2 , and C_3 species is presented by Kathrotia et al. [26]. The non-premixed flames are simulated in one-dimensional geometry using the INSFLA flame code [27, 28], which requires as input the initial mixture composition, pressure, temperature at the burner surface, fuel exit velocity, and strain rate. As discussed in [29], the disadvantage of using measured temperature profiles as input for the simulation is that for non-premixed flames the resulting calculated reaction zones sometimes show unrealistic flame structures. Therefore, in the present modeling approach temperature profiles were calculated from the energy balance. Although not discussed in detail here, for the flames investigated in this work the calculated temperature profiles were validated by N_2 -CARS thermometry [24] and showed good agreement with experiments.

4 Results and discussion

4.1 CH_4/air flames (type I)

It is expected that the CL-intensity profiles are spatially narrow and located near the zone of steepest temperature gradient. Because flame conditions do not change along the line-of-sight of the detection system (cf. Fig. 1), simulated CL

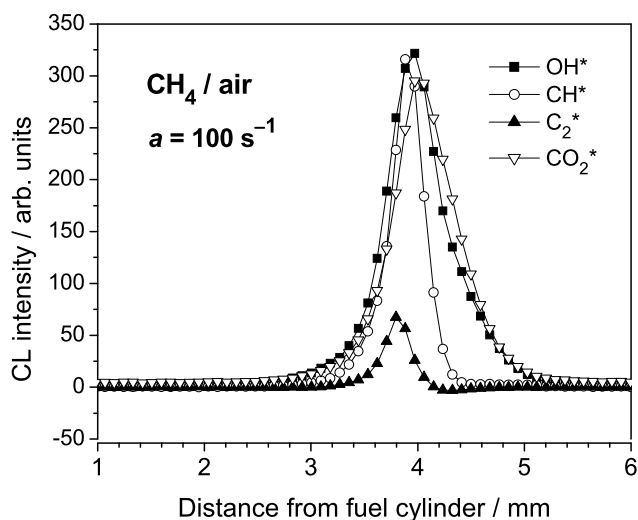


Fig. 4 Species-specific spatial CL-intensity profiles evaluated from the selected band intensities (cf. Fig. 3) of OH* (solid squares), CH* (open circles), C₂* (solid triangles), and CO₂* (open triangles) for the type I flame with a strain rate of 100 s⁻¹

species profiles are compared with the pixel counts along the spectrometer slit height spectrally integrated within the respective emission band of each species (cf. Fig. 3). However, imperfections of the imaging system (spherical and chromatic aberrations, finite sensor pixel size) and image blurring due to the extended luminous flame zone along the line-of-sight lead to broadening of the profiles (see Sect. 2.2.2), which needs to be kept in mind when comparisons are made to simulation results.

For the case of a strain rate of $a = 100 \text{ s}^{-1}$, Fig. 4 presents the evaluated spatial profiles of the species-specific CL-band intensities as a function of distance from the sintered metal cylinder that acts as the source of the gaseous fuel. Within the spatial resolution of the imaging/detection system the OH* and CO₂* profiles attain their maxima at about 4.0 mm from the burner head, while the CH* and C₂* profiles peak at slightly smaller values (3.9 and 3.8 mm, respectively).

Figure 5 shows the CL profiles of OH* and CH* as a function of strain rate (the C₂* and CO₂* profiles show similar behavior). Curves with symbols are experimental data, while the filled-in profiles are simulation results. For better comparison, in each panel the peak value of the experimental intensity profile for the lowest strain rate case of $a = 100 \text{ s}^{-1}$ has been normalized to the respective simulated peak mole fraction, and all other experimental profiles in the same plot were multiplied by the same scaling factor. It is observed that with increasing strain rate, all peak intensities increase (more strongly for OH* than for CH*), the profiles shift closer to the burner head (cf. Fig. 6), and their respective spatial widths (measured as-

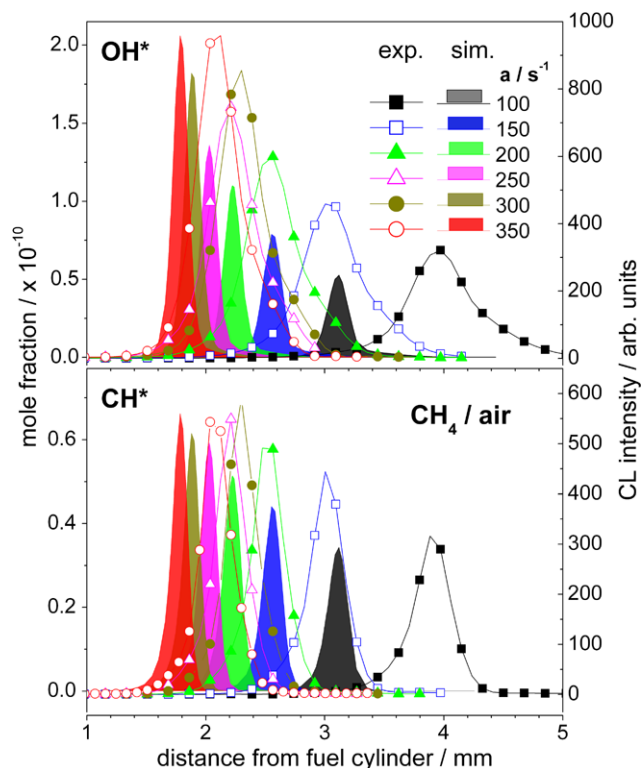


Fig. 5 Measured CL-intensity profiles (symbols with solid lines) and modeled mole-fraction profiles (filled-in curves) of OH* (upper graph) and CH* (lower graph) for the type I flames for various strain rates a . See text for further explanations

FWHM) slightly decrease. It must be emphasized that these trends are valid for the measured profiles of the flames with $a = 100\text{--}250 \text{ s}^{-1}$, and then again for the $a = 300$ and 350 s^{-1} flames, since for the two highest strain rates a larger fuel flow rate was used (cf. Table 1) to avoid extinction of the flames when approaching the sintered cylinder surface. This change in fuel flow rate causes a non-monotonic shift in the profile peak position. Inspection of the profiles in Fig. 5 also reveals that for the same flame conditions the experimental CH* profiles are narrower than those of OH*, which is not so obvious in the respective simulated mole-fraction profiles. However, in general the simulated profiles are between a factor of 1.9 (C₂*, $a = 150 \text{ s}^{-1}$) and 3 (OH*, $a = 150 \text{ s}^{-1}$) smaller in width than the experimental ones. For the main part this is ascribed to the limited spatial resolution of the imaging system and the diffuse background contribution from the out-of-focus CL radiation from the flames. From Fig. 2 the smallest measured profile FWHM is around 220 μm , almost equal to the previously estimated optical spatial resolution of the present imaging system.

Figure 6 illustrates the general trends of peak intensity and peak position for OH*, CH*, and C₂* for all type I flames obtained from experiment (filled symbols,

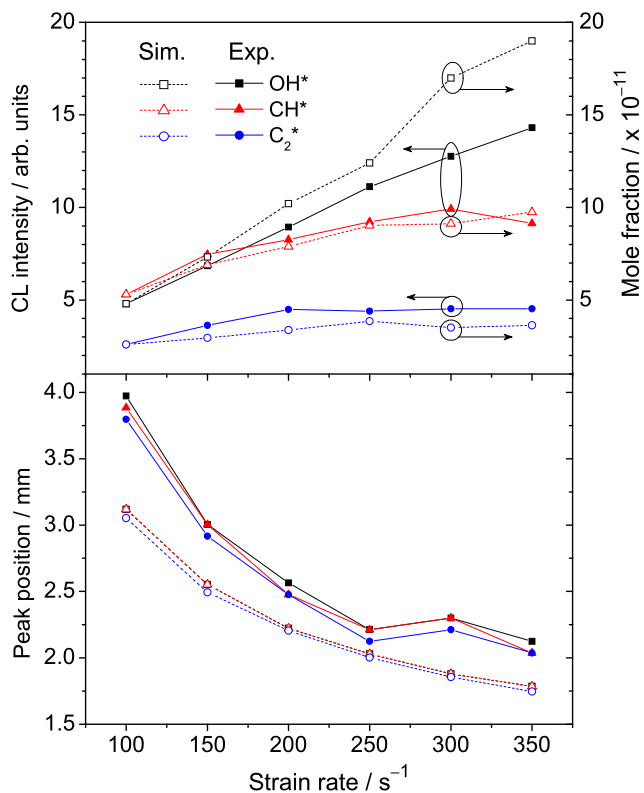


Fig. 6 Upper panel: measured peak CL intensities (filled symbols and solid lines, left-hand axis) and the respective simulated peak mole fractions (open symbols and dashed lines, right-hand axis), in the type I flames as a function of strain rate. The CL intensities are normalized to the respective model parameters for the $a = 100 \text{ s}^{-1}$ flame. Lower panel: respective peak positions

solid lines) and simulation (open symbols, dashed lines), respectively.

For OH^* , the increase of the CL intensity with strain rate is in accord with findings by De Leo et al. [5] in a flat counterflow flame, although in their experiments strain rates were much lower (between 20 and 40 s^{-1}). The same trends are seen in Fig. 6 (upper panel) for the other species investigated, with those for C_2^* being the least pronounced. As is also shown in Fig. 6 (upper panel), if the measured CL peak intensities are normalized to the respective mole-fraction values for the $a = 100 \text{ s}^{-1}$ flame from the simulations, the general trends with strain rate are in good overall agreement between simulation and experiment, except for the case of OH^* , where the values diverge with increasing strain rate. For the simulations the species profiles generally peak at smaller distances from the fuel cylinder (lower panel in Fig. 6), most strongly deviating from the measurements for strain rates smaller than 200 s^{-1} . These discrepancies cannot solely be attributed to uncertainties in experimental flow settings, since a $\pm 20\%$ variation in the nominal value of the fuel ejection velocity (cf. Table 1) changed the simulated profile positions by less than 0.15 mm.

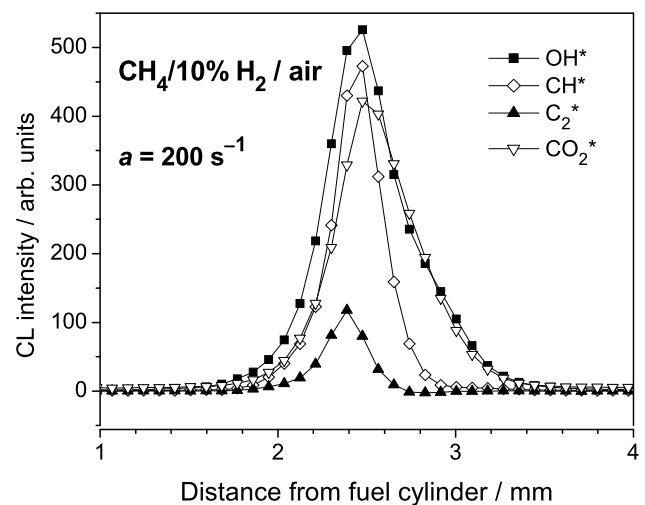


Fig. 7 Species-specific spatial CL profiles evaluated from the selected band intensities of OH^* (solid squares), CH^* (open diamonds), C_2^* (solid triangles), and CO_2^* (open triangles) for a type II flame with a strain rate of 200 s^{-1} and 10 % (by vol.) H_2 in the fuel

4.2 $\text{CH}_4/\text{H}_2/\text{air}$ flames (type II)

Figure 7 presents the evaluated CL-intensity profiles of all detected species for a type II flame with $a = 200 \text{ s}^{-1}$, when 10 % (by vol.) H_2 replaces an equal amount of CH_4 , keeping the total volumetric fuel flow through the burner head constant at 3 slpm (corresponding to a fuel ejection velocity of 0.16 m/s). At this H_2 content the shapes and relative intensities of the individual species profiles behave similarly to the ones recorded in the pure methane flames (cf. Fig. 4), although the CH^* and CO_2^* peak intensities dropped somewhat more in relation to the OH^* signal.

The changes with increasing fuel hydrogen content of the measured OH^* and CH^* CL profiles are depicted in Fig. 8 (open symbols with solid lines). For better comparison with the modeled mole-fraction profiles (filled-in curves in Fig. 8), the intensity profile for the 0 % H_2 case was normalized to the respective simulated profile. With increasing H_2 content for both species the measured CL maxima decrease (by about 33 % for OH^* and 18 % for CH^*) and their peak positions slightly shift closer to the fuel cylinder (cf. Fig. 9). This is in striking contrast to the simulated profiles (filled-in curves in Fig. 8), where the peaks shift away from the fuel side and the decrease in concentration of the respective CL species is much stronger for increasing H_2 fraction.

For the type II flames, Fig. 9 summarizes the variation of the peak intensities (upper panel) and peak positions (lower panel) of the respective CL species with increasing H_2 content in the fuel, from both experiment (solid symbols and lines) and simulation (open symbols and dashed lines).

Because in the present experiments CL-signal intensities are in arbitrary units, the same as in Fig. 6, the measured

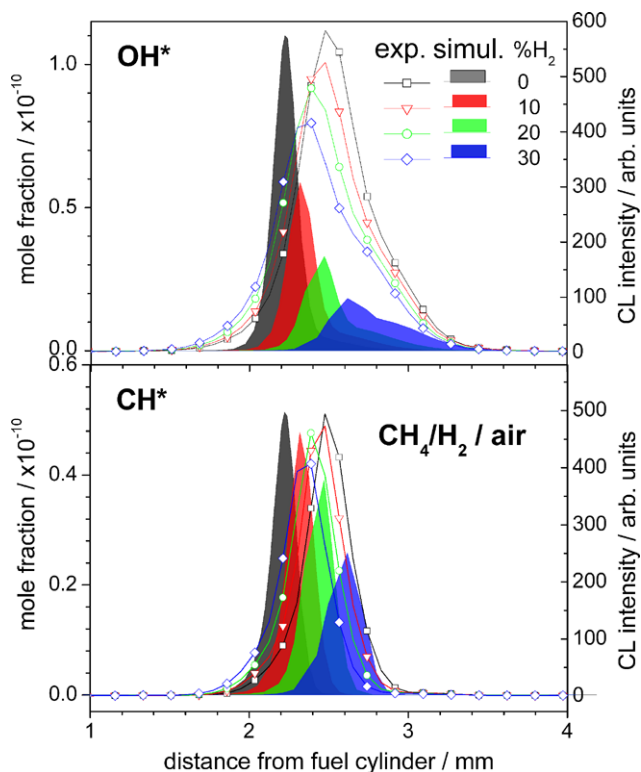


Fig. 8 Measured CL-intensity (symbols with solid lines) and modeled mole-fraction profiles (filled-in curves) of OH* (upper graph) and CH* (lower graph) for type II flames for a strain rate of 200 s^{-1} and variable H₂ content in the fuel. See text for details

CL-intensity maxima are normalized to the respective simulated species mole fractions for the case with no H₂ in the fuel, and scaled accordingly for the other fuel mixtures (upper panel). Starting with the pure CH₄ case, with increasing H₂ content the experimental CL intensities of OH* and CH* decrease, while the C₂* peak intensity stays almost constant within the experimental uncertainty. As mentioned above, with the exception of the C₂* mole fraction this is in contrast with the model results (open symbols and dashed lines) where the intensity decreases much more strongly with increasing H₂ concentration in the fuel. At the same time the measured profiles slightly shift towards the fuel cylinder, almost opposite to what is predicted by the simulations (lower panel in Fig. 9). In addition, the half widths of the profiles (not shown in Fig. 9) increase slightly (for OH*) with increasing H₂ content in the fuel, while those of CH* and C₂*, being narrower by roughly a factor of 1.5–2, stay almost constant.

5 Conclusions

In the present work non-premixed counterflow flames of the ‘Tsuji type’, i.e. stabilized in the forward stagnation region of a fuel flow exiting through the wall of a sintered cylinder

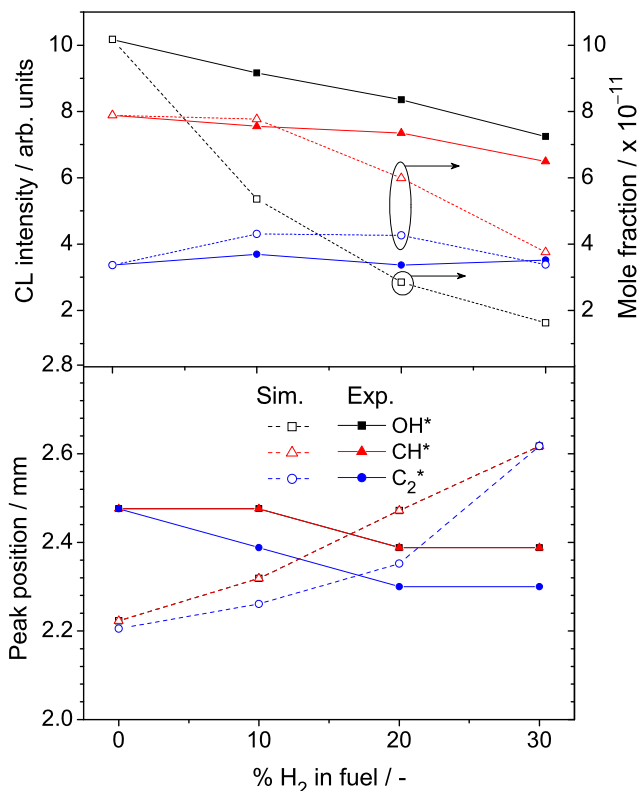


Fig. 9 Upper panel: measured peak CL-intensities (filled symbols and solid lines) and respective simulated peak mole fractions (open symbols and dashed lines, right-hand axis), in type II flames as a function of H₂ content in the fuel. The CL intensities are normalized to the respective simulation results for the 0 % H₂ case. Lower panel: respective peak positions

and a uniform air stream in a counterpropagating direction, were analyzed experimentally and through detailed modeling with respect to their chemiluminescence (CL) emission and mole-fraction profiles, respectively. The flame front of these flames stands off a fixed distance from the fuel cylinder, enabling the acquisition of spatially resolved CL profiles by imaging with a large depth-of-field imaging optics through a spectrometer onto a CCD camera, and evaluating the CL spectral bands individually. Simulations were performed with an in-house kinetics mechanism comprising elementary reactions up to C₄ hydrocarbons under non-sooting conditions, formation and removal/destruction of electronically excited species, and an updated thermochemical database. For flames with pure CH₄ as fuel the measured trends of CL profile peak intensities and shifts with increasing strain rate are captured quite well in the simulation; however, the simulated species profiles peak at consistently smaller distances from the fuel cylinder than was measured. Stronger discrepancies are observed, however, for flames with increasing amounts of H₂ (up to 30 %) in the fuel, where, in contrast to the experimental findings, simulated peaks of CL mole-fraction profiles decrease much

more strongly and shift away from the fuel cylinder with more H₂ in the fuel.

Future work needs to also incorporate the distortions (i.e. broadening) of the modeled CL profiles due to the limited spatial resolution attainable experimentally through the combination of the optical imaging and detection systems. This could be achieved by a proper convolution of the model profiles with the instrumental point-spread function determined experimentally in a similar way as presented here (cf. Fig. 2). The spatial resolution of the imaging system could also be improved by, for example, a distance microscope.

Acknowledgements The authors acknowledge funding of this work by the Deutsche Forschungsgemeinschaft (DFG) within the collaborative program ‘Chemilumineszenz und Wärmefreisetzung’.

References

1. H. Tsuji, I. Yamaoka, Proc. Combust. Inst. **13**, 723 (1971)
2. M.D. Smooke, I.K. Puri, K. Seshadri, Proc. Combust. Inst. **21**, 1783 (1986)
3. R.S. Barlow, A.N. Karpetis, J.H. Frank, J.-Y. Chen, Combust. Flame **127**, 2102 (2001)
4. G. Dixon-Lewis, T. David, P.H. Gaskell, S. Fukutani, H. Jinno, J.A. Miller, R.J. Kee, M.D. Smooke, N. Peters, E. Effelsberg, J. Warnatz, F. Behrendt, Proc. Combust. Inst. **20**, 1893 (1984)
5. M. De Leo, A. Saveliev, L.A. Kennedy, S.A. Zelepouga, Combust. Flame **149**, 435 (2007)
6. F.A. Williams, in *Turbulent Mixing in Non-reactive and Reactive Flows*, ed. by S.N.B. Murthy (Plenum, New York, 1974), p. 189
7. I. Yamaoka, H. Tsuji, Proc. Combust. Inst. **16**, 1145 (1977)
8. F. Akamatsu, T. Wakabayashi, S. Tsushima, Y. Mizutani, Y. Ikeda, N. Kawahara, T. Nakajima, Meas. Sci. Technol. **10**, 1240 (1999)
9. Y. Hardalupas, C.S. Panoutsos, A.M.K.P. Taylor, Exp. Fluids **49**, 883 (2010)
10. Y. Hardalupas, M. Orain, Combust. Flame **139**, 188 (2004)
11. C.S. Panoutsos, Y. Hardalupas, A.M.K.P. Taylor, Combust. Flame **156**, 273 (2009)
12. V.N. Nori, J.M. Seitzman, in *45th AIAA Aerospace Sciences Meet. Exhib.*, Reno, NV (2007)
13. F.V. Tinaut, M. Reyes, B. Giménez, J.V. Pastor, Energy Fuels **25**, 119 (2011)
14. T.S. Cheng, C.-Y. Wu, Y.-H. Li, Y.-C. Chao, Combust. Sci. Technol. **178**, 1821 (2006)
15. N. Docquier, S. Belhafaoui, F. Lacas, N. Darabiha, C. Rolon, Proc. Combust. Inst. **28**, 1765 (2000)
16. J. Kojima, Y. Ikeda, T. Nakajima, Proc. Combust. Inst. **28**, 1757 (2000)
17. D. Dandy, S. Vosen, Combust. Sci. Technol. **82**, 131 (1992)
18. K.T. Walsh, M.B. Long, M.A. Tanoff, M.D. Smooke, Proc. Combust. Inst. **27**, 615 (1998)
19. J. Luque, J.B. Jeffries, G.P. Smith, D.R. Crosley, K.T. Walsh, M.B. Long, M.D. Smooke, Combust. Flame **122**, 172 (2000)
20. J.-M. Samaniego, F.N. Egolfopoulos, C.T. Bowman, Combust. Sci. Technol. **109**, 183 (1995)
21. H. Tsuji, Prog. Energy Combust. Sci. **8**, 93 (1982)
22. A.G. Gaydon, H.G. Wolfhard, *Flames: Their Structure, Radiation, and Temperature* (Chapman and Hall, London, 1978)
23. M. Slack, A. Grillo, Combust. Flame **59**, 189 (1985)
24. T. Kathrotia, PhD thesis, Naturwissenschaftlich-Mathematische Gesamtfakultät, Universität Heidelberg (2011). Available online: <http://archiv.ub.uniheidelberg.de/volltextserver/volltexte/2011/12027>
25. E. Goos, A. Burcat, B. Ruscic, Rep. ANL 05/20 TAE 960 (2011)
26. T. Kathrotia, U. Riedel, A. Seipel, K. Moshhammer, A. Brockhinke, Appl. Phys. B (this issue)
27. U. Maas, Appl. Math. **40**, 249 (1995)
28. U. Maas, J. Warnatz, Combust. Flame **74**, 53 (1988)
29. J.J. Driscoll, University of Michigan, Department of Mechanical Engineering, Ann Arbor, MI, USA (2002)